

Search for the rare decay $B_s^0 \rightarrow \mu^+ \mu^-$

V.M. Abazov,³² B. Abbott,⁶⁷ B.S. Acharya,²⁶ M. Adams,⁴⁶ T. Adams,⁴⁴ G.D. Alexeev,³² G. Alkhazov,³⁶
A. Alton^{a,56} A. Askew,⁴⁴ S. Atkins,⁵⁴ K. Augsten,⁷ C. Avila,⁵ F. Badaud,¹⁰ L. Bagby,⁴⁵ B. Baldin,⁴⁵
D.V. Bandurin,⁴⁴ S. Banerjee,²⁶ E. Barberis,⁵⁵ P. Baringer,⁵³ J.F. Bartlett,⁴⁵ U. Bassler,¹⁵ V. Bazterra,⁴⁶
A. Bean,⁵³ M. Begalli,² L. Bellantoni,⁴⁵ S.B. Beri,²⁴ G. Bernardi,¹⁴ R. Bernhard,¹⁹ I. Bertram,³⁹ M. Besançon,¹⁵
R. Beuselinck,⁴⁰ P.C. Bhat,⁴⁵ S. Bhatia,⁵⁸ V. Bhatnagar,²⁴ G. Blazey,⁴⁷ S. Blessing,⁴⁴ K. Bloom,⁵⁹ A. Boehnlein,⁴⁵
D. Boline,⁶⁴ E.E. Boos,³⁴ G. Borissov,³⁹ A. Brandt,⁷⁰ O. Brandt,²⁰ R. Brock,⁵⁷ A. Bross,⁴⁵ D. Brown,¹⁴
X.B. Bu,⁴⁵ M. Buehler,⁴⁵ V. Buescher,²¹ V. Bunichev,³⁴ S. Burdin,^{b,39} C.P. Buszello,³⁸ E. Camacho-Pérez,²⁹
B.C.K. Casey,⁴⁵ H. Castilla-Valdez,²⁹ S. Caughron,⁵⁷ S. Chakrabarti,⁶⁴ D. Chakraborty,⁴⁷ K.M. Chan,⁵¹
A. Chandra,⁷² E. Chapon,¹⁵ G. Chen,⁵³ S.W. Cho,²⁸ S. Choi,²⁸ B. Choudhary,²⁵ S. Cihangir,⁴⁵ D. Claes,⁵⁹
J. Clutter,⁵³ M. Cooke,⁴⁵ W.E. Cooper,⁴⁵ M. Corcoran,⁷² F. Couderc,¹⁵ M.-C. Cousinou,¹² D. Cutts,⁶⁹ A. Das,⁴²
G. Davies,⁴⁰ S.J. de Jong,^{30,31} E. De La Cruz-Burelo,²⁹ F. Déliot,¹⁵ R. Demina,⁶³ D. Denisov,⁴⁵ S.P. Denisov,³⁵
S. Desai,⁴⁵ C. Deterre,^{d,20} K. DeVaughan,⁵⁹ H.T. Diehl,⁴⁵ M. Diesburg,⁴⁵ P.F. Ding,⁴¹ A. Dominguez,⁵⁹ A. Dubey,²⁵
L.V. Dudko,³⁴ A. Duperrin,¹² S. Dutt,²⁴ A. Dyshkant,⁴⁷ M. Eads,⁴⁷ D. Edmunds,⁵⁷ J. Ellison,⁴³ V.D. Elvira,⁴⁵
Y. Enari,¹⁴ H. Evans,⁴⁹ V.N. Evdokimov,³⁵ L. Feng,⁴⁷ T. Ferbel,⁶³ F. Fiedler,²¹ F. Filthaut,^{30,31} W. Fisher,⁵⁷
H.E. Fisk,⁴⁵ M. Fortner,⁴⁷ H. Fox,³⁹ S. Fuess,⁴⁵ P. H. Garbincius,⁴⁵ A. Garcia-Bellido,⁶³ J.A. García-González,²⁹
G.A. García-Guerra,^{c,29} V. Gavrilov,³³ W. Geng,^{12,57} C.E. Gerber,⁴⁶ Y. Gershtein,⁶⁰ G. Ginther,^{45,63}
G. Golovanov,³² P.D. Grannis,⁶⁴ S. Greder,¹⁶ H. Greenlee,⁴⁵ G. Grenier,¹⁷ Ph. Gris,¹⁰ J.-F. Grivaz,¹³
A. Grohsjean,^{d,15} S. Grünendahl,⁴⁵ M.W. Grünewald,²⁷ T. Guillemin,¹³ G. Gutierrez,⁴⁵ P. Gutierrez,⁶⁷ J. Haley,⁵⁵
L. Han,⁴ K. Harder,⁴¹ A. Harel,⁶³ J.M. Hauptman,⁵² J. Hays,⁴⁰ T. Head,⁴¹ T. Hebbeker,¹⁸ D. Hedin,⁴⁷ H. Hegab,⁶⁸
A.P. Heinson,⁴³ U. Heintz,⁶⁹ C. Hensel,²⁰ I. Heredia-De La Cruz,²⁹ K. Herner,⁵⁶ G. Hesketh,^{f,41} M.D. Hildreth,⁵¹
R. Hirosky,⁷³ T. Hoang,⁴⁴ J.D. Hobbs,⁶⁴ B. Hoeneisen,⁹ J. Hogan,⁷² M. Hohlfeld,²¹ I. Howley,⁷⁰ Z. Hubacek,^{7,15}
V. Hynek,⁷ I. Iashvili,⁶² Y. Ilchenko,⁷¹ R. Illingworth,⁴⁵ A.S. Ito,⁴⁵ S. Jabeen,⁶⁹ M. Jaffré,¹³ A. Jayasinghe,⁶⁷
M.S. Jeong,²⁸ R. Jesik,⁴⁰ P. Jiang,⁴ K. Johns,⁴² E. Johnson,⁵⁷ M. Johnson,⁴⁵ A. Jonckheere,⁴⁵ P. Jonsson,⁴⁰
J. Joshi,⁴³ A.W. Jung,⁴⁵ A. Juste,³⁷ E. Kajfasz,¹² D. Karmanov,³⁴ I. Katsanos,⁵⁹ R. Kehoe,⁷¹ S. Kermiche,¹²
N. Khalatyan,⁴⁵ A. Khanov,⁶⁸ A. Kharchilava,⁶² Y.N. Kharzheev,³² I. Kiselevich,³³ J.M. Kohli,²⁴ A.V. Kozelov,³⁵
J. Kraus,⁵⁸ A. Kumar,⁶² A. Kupco,⁸ T. Kurča,¹⁷ V.A. Kuzmin,³⁴ S. Lammers,⁴⁹ P. Lebrun,¹⁷ H.S. Lee,²⁸
S.W. Lee,⁵² W.M. Lee,⁴⁴ X. Lei,⁴² J. Lellouch,¹⁴ D. Li,¹⁴ H. Li,⁷³ L. Li,⁴³ Q.Z. Li,⁴⁵ J.K. Lim,²⁸ D. Lincoln,⁴⁵
J. Linnemann,⁵⁷ V.V. Lipaev,³⁵ R. Lipton,⁴⁵ H. Liu,⁷¹ Y. Liu,⁴ A. Lobodenko,³⁶ M. Lokajicek,⁸ R. Lopes de Sa,⁶⁴
R. Luna-Garcia,^{g,29} A.L. Lyon,⁴⁵ A.K.A. Maciel,¹ R. Magaña-Villalba,²⁹ S. Malik,⁵⁹ V.L. Malyshev,³² J. Mansour,²⁰
J. Martínez-Ortega,²⁹ R. McCarthy,⁶⁴ C.L. McGivern,⁴¹ M.M. Meijer,^{30,31} A. Melnitchouk,⁴⁵ D. Menezes,⁴⁷
P.G. Mercadante,³ M. Merkin,³⁴ A. Meyer,¹⁸ J. Meyer,^{j,20} F. Miconi,¹⁶ N.K. Mondal,²⁶ M. Mulhearn,⁷³ E. Nagy,¹²
M. Naimuddin,²⁵ M. Narain,⁶⁹ R. Nayyar,⁴² H.A. Neal,⁵⁶ J.P. Negret,⁵ P. Neustroev,³⁶ H.T. Nguyen,⁷³
T. Nunnemann,²² J. Orduna,⁷² N. Osman,¹² J. Osta,⁵¹ M. Padilla,⁴³ A. Pal,⁷⁰ N. Parashar,⁵⁰ V. Parihar,⁶⁹
S.K. Park,²⁸ R. Partridge,^{e,69} N. Parua,⁴⁹ A. Patwa,^{k,65} B. Penning,⁴⁵ M. Perfilov,³⁴ Y. Peters,²⁰ K. Petridis,⁴¹
G. Petrillo,⁶³ P. Pétroff,¹³ M.-A. Pleier,⁶⁵ P.L.M. Podesta-Lerma,^{h,29} V.M. Podstavkov,⁴⁵ A.V. Popov,³⁵
M. Prewitt,⁷² D. Price,⁴⁹ N. Prokopenko,³⁵ J. Qian,⁵⁶ A. Quadt,²⁰ B. Quinn,⁵⁸ M.S. Rangel,¹ P.N. Ratoff,³⁹
I. Razumov,³⁵ I. Ripp-Baudot,¹⁶ F. Rizatdinova,⁶⁸ M. Rominsky,⁴⁵ A. Ross,³⁹ C. Royon,¹⁵ P. Rubinov,⁴⁵
R. Ruchti,⁵¹ G. Sajot,¹¹ P. Salcido,⁴⁷ A. Sánchez-Hernández,²⁹ M.P. Sanders,²² A.S. Santos,^{i,1} G. Savage,⁴⁵
L. Sawyer,⁵⁴ T. Scanlon,⁴⁰ R.D. Schamberger,⁶⁴ Y. Scheglov,³⁶ H. Schellman,⁴⁸ C. Schwanenberger,⁴¹
R. Schwienhorst,⁵⁷ J. Sekaric,⁵³ H. Severini,⁶⁷ E. Shabalina,²⁰ V. Shary,¹⁵ S. Shaw,⁵⁷ A.A. Shchukin,³⁵
R.K. Shivpuri,²⁵ V. Simak,⁷ P. Skubic,⁶⁷ P. Slattery,⁶³ D. Smirnov,⁵¹ K.J. Smith,⁶² G.R. Snow,⁵⁹ J. Snow,⁶⁶
S. Snyder,⁶⁵ S. Söldner-Rembold,⁴¹ L. Sonnenschein,¹⁸ K. Soustruznik,⁶ J. Stark,¹¹ D.A. Stoyanova,³⁵ M. Strauss,⁶⁷
L. Suter,⁴¹ P. Svoisky,⁶⁷ M. Titov,¹⁵ V.V. Tokmenin,³² Y.-T. Tsai,⁶³ D. Tsybychev,⁶⁴ B. Tuchming,¹⁵ C. Tully,⁶¹
L. Uvarov,³⁶ S. Uvarov,³⁶ S. Uzunyan,⁴⁷ R. Van Kooten,⁴⁹ W.M. van Leeuwen,³⁰ N. Varelas,⁴⁶ E.W. Varnes,⁴²
I.A. Vasilyev,³⁵ A.Y. Verkheev,³² L.S. Vertogradov,³² M. Verzocchi,⁴⁵ M. Vesterinen,⁴¹ D. Vilanova,¹⁵ P. Vokac,⁷
H.D. Wahl,⁴⁴ M.H.L.S. Wang,⁴⁵ J. Warchol,⁵¹ G. Watts,⁷⁴ M. Wayne,⁵¹ J. Weichert,²¹ L. Welty-Rieger,⁴⁸
A. White,⁷⁰ D. Wicke,²³ M.R.J. Williams,³⁹ G.W. Wilson,⁵³ M. Wobisch,⁵⁴ D.R. Wood,⁵⁵ T.R. Wyatt,⁴¹ Y. Xie,⁴⁵
R. Yamada,⁴⁵ S. Yang,⁴ T. Yasuda,⁴⁵ Y.A. Yatsunenko,³² W. Ye,⁶⁴ Z. Ye,⁴⁵ H. Yin,⁴⁵ K. Yip,⁶⁵ S.W. Youn,⁴⁵
J.M. Yu,⁵⁶ J. Zennamo,⁶² T.G. Zhao,⁴¹ B. Zhou,⁵⁶ J. Zhu,⁵⁶ M. Zielinski,⁶³ D. Zieminska,⁴⁹ and L. Zivkovic¹⁴

(The D0 Collaboration*)

- ¹LAFEX, Centro Brasileiro de Pesquisas Físicas, Rio de Janeiro, Brazil
- ²Universidade do Estado do Rio de Janeiro, Rio de Janeiro, Brazil
- ³Universidade Federal do ABC, Santo André, Brazil
- ⁴University of Science and Technology of China, Hefei, People's Republic of China
- ⁵Universidad de los Andes, Bogotá, Colombia
- ⁶Charles University, Faculty of Mathematics and Physics,
Center for Particle Physics, Prague, Czech Republic
- ⁷Czech Technical University in Prague, Prague, Czech Republic
- ⁸Center for Particle Physics, Institute of Physics,
Academy of Sciences of the Czech Republic, Prague, Czech Republic
- ⁹Universidad San Francisco de Quito, Quito, Ecuador
- ¹⁰LPC, Université Blaise Pascal, CNRS/IN2P3, Clermont, France
- ¹¹LPSC, Université Joseph Fourier Grenoble 1, CNRS/IN2P3,
Institut National Polytechnique de Grenoble, Grenoble, France
- ¹²CPPM, Aix-Marseille Université, CNRS/IN2P3, Marseille, France
- ¹³LAL, Université Paris-Sud, CNRS/IN2P3, Orsay, France
- ¹⁴LPNHE, Universités Paris VI and VII, CNRS/IN2P3, Paris, France
- ¹⁵CEA, Irfu, SPP, Saclay, France
- ¹⁶IPHC, Université de Strasbourg, CNRS/IN2P3, Strasbourg, France
- ¹⁷IPNL, Université Lyon 1, CNRS/IN2P3, Villeurbanne, France and Université de Lyon, Lyon, France
- ¹⁸III. Physikalisches Institut A, RWTH Aachen University, Aachen, Germany
- ¹⁹Physikalisches Institut, Universität Freiburg, Freiburg, Germany
- ²⁰II. Physikalisches Institut, Georg-August-Universität Göttingen, Göttingen, Germany
- ²¹Institut für Physik, Universität Mainz, Mainz, Germany
- ²²Ludwig-Maximilians-Universität München, München, Germany
- ²³Fachbereich Physik, Bergische Universität Wuppertal, Wuppertal, Germany
- ²⁴Panjab University, Chandigarh, India
- ²⁵Delhi University, Delhi, India
- ²⁶Tata Institute of Fundamental Research, Mumbai, India
- ²⁷University College Dublin, Dublin, Ireland
- ²⁸Korea Detector Laboratory, Korea University, Seoul, Korea
- ²⁹CINVESTAV, Mexico City, Mexico
- ³⁰Nikhef, Science Park, Amsterdam, the Netherlands
- ³¹Radboud University Nijmegen, Nijmegen, the Netherlands
- ³²Joint Institute for Nuclear Research, Dubna, Russia
- ³³Institute for Theoretical and Experimental Physics, Moscow, Russia
- ³⁴Moscow State University, Moscow, Russia
- ³⁵Institute for High Energy Physics, Protvino, Russia
- ³⁶Petersburg Nuclear Physics Institute, St. Petersburg, Russia
- ³⁷Institució Catalana de Recerca i Estudis Avançats (ICREA) and Institut de Física d'Altes Energies (IFAE), Barcelona, Spain
- ³⁸Uppsala University, Uppsala, Sweden
- ³⁹Lancaster University, Lancaster LA1 4YB, United Kingdom
- ⁴⁰Imperial College London, London SW7 2AZ, United Kingdom
- ⁴¹The University of Manchester, Manchester M13 9PL, United Kingdom
- ⁴²University of Arizona, Tucson, Arizona 85721, USA
- ⁴³University of California Riverside, Riverside, California 92521, USA
- ⁴⁴Florida State University, Tallahassee, Florida 32306, USA
- ⁴⁵Fermi National Accelerator Laboratory, Batavia, Illinois 60510, USA
- ⁴⁶University of Illinois at Chicago, Chicago, Illinois 60607, USA
- ⁴⁷Northern Illinois University, DeKalb, Illinois 60115, USA
- ⁴⁸Northwestern University, Evanston, Illinois 60208, USA
- ⁴⁹Indiana University, Bloomington, Indiana 47405, USA
- ⁵⁰Purdue University Calumet, Hammond, Indiana 46323, USA
- ⁵¹University of Notre Dame, Notre Dame, Indiana 46556, USA
- ⁵²Iowa State University, Ames, Iowa 50011, USA
- ⁵³University of Kansas, Lawrence, Kansas 66045, USA
- ⁵⁴Louisiana Tech University, Ruston, Louisiana 71272, USA
- ⁵⁵Northeastern University, Boston, Massachusetts 02115, USA
- ⁵⁶University of Michigan, Ann Arbor, Michigan 48109, USA
- ⁵⁷Michigan State University, East Lansing, Michigan 48824, USA
- ⁵⁸University of Mississippi, University, Mississippi 38677, USA
- ⁵⁹University of Nebraska, Lincoln, Nebraska 68588, USA

- ⁶⁰Rutgers University, Piscataway, New Jersey 08855, USA
⁶¹Princeton University, Princeton, New Jersey 08544, USA
⁶²State University of New York, Buffalo, New York 14260, USA
⁶³University of Rochester, Rochester, New York 14627, USA
⁶⁴State University of New York, Stony Brook, New York 11794, USA
⁶⁵Brookhaven National Laboratory, Upton, New York 11973, USA
⁶⁶Langston University, Langston, Oklahoma 73050, USA
⁶⁷University of Oklahoma, Norman, Oklahoma 73019, USA
⁶⁸Oklahoma State University, Stillwater, Oklahoma 74078, USA
⁶⁹Brown University, Providence, Rhode Island 02912, USA
⁷⁰University of Texas, Arlington, Texas 76019, USA
⁷¹Southern Methodist University, Dallas, Texas 75275, USA
⁷²Rice University, Houston, Texas 77005, USA
⁷³University of Virginia, Charlottesville, Virginia 22904, USA
⁷⁴University of Washington, Seattle, Washington 98195, USA

(Dated: January 18, 2013)

We perform a search for the rare decay $B_s^0 \rightarrow \mu^+ \mu^-$ using data collected by the D0 experiment at the Fermilab Tevatron Collider. This result is based on the full D0 Run II dataset corresponding to 10.4 fb^{-1} of $p\bar{p}$ collisions at $\sqrt{s} = 1.96 \text{ TeV}$. We use a multivariate analysis to increase the sensitivity of the search. In the absence of an observed number of events above the expected background, we set an upper limit on the decay branching fraction of $\mathcal{B}(B_s^0 \rightarrow \mu^+ \mu^-) < 15 \times 10^{-9}$ at the 95% C.L.

PACS numbers: 13.20.He, 14.40.Nd

I. INTRODUCTION

The rare decay $B_s^0 \rightarrow \mu^+ \mu^-$ is highly suppressed in the standard model (SM) due to its flavor changing neutral current (FCNC) nature. FCNC decays can only proceed in the SM through higher-order diagrams as shown in Fig. 1. This decay is further suppressed due to the required helicities of the final state muons in the decay of the spin zero B_s^0 meson. Recent improvements in the SM prediction for the branching fraction $\mathcal{B}(B_s^0 \rightarrow \mu^+ \mu^-)$ include the effect of the non-zero lifetime difference $\Delta\Gamma_s$ between the heavy and light mass eigenstates of the B_s^0 meson [1, 2], resulting in an expected branching fraction of $(3.5 \pm 0.2) \times 10^{-9}$, which is about 10% larger than previous calculations [3].

Several scenarios of physics beyond the standard model (BSM) predict significant enhancements of this decay channel [4–6], making the study of this process a promising way to search for new physics. However, it is also possible in some BSM scenarios for this decay to be suppressed even further than the SM prediction [7].

Previous D0 experiment 95% C.L. limits on the branching fraction for $B_s^0 \rightarrow \mu^+ \mu^-$ include a limit of

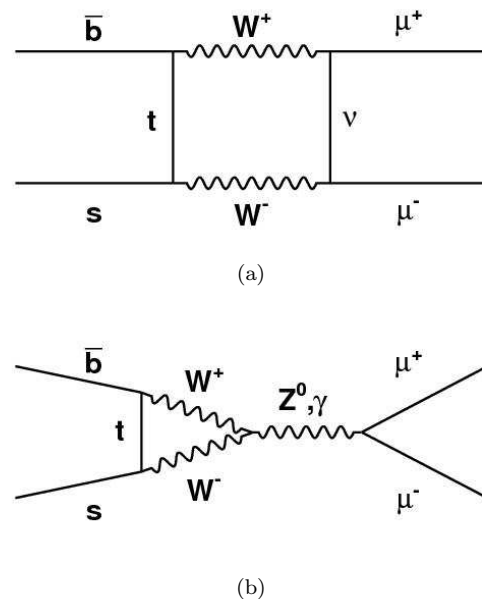


FIG. 1: The (a) box diagram and (b) electroweak penguin diagram are examples of the FCNC processes through which the decay $B_s^0 \rightarrow \mu^+ \mu^-$ can proceed.

*with visitors from ^aAugustana College, Sioux Falls, SD, USA, ^bThe University of Liverpool, Liverpool, UK, ^cUPIITA-IPN, Mexico City, Mexico, ^dDESY, Hamburg, Germany, ^eSLAC, Menlo Park, CA, USA, ^fUniversity College London, London, UK, ^gCentro de Investigacion en Computacion - IPN, Mexico City, Mexico, ^hECFM, Universidad Autonoma de Sinaloa, Culiacán, Mexico, ⁱUniversidade Estadual Paulista, São Paulo, Brazil, ^jKarlsruher Institut für Technologie (KIT) - Steinbuch Centre for Computing (SCC) and ^kOffice of Science, U.S. Department of Energy, Washington, D.C. 20585, USA.

5×10^{-7} from a cut-based analysis using 240 pb^{-1} of integrated luminosity [8]; a limit of 1.2×10^{-7} from a likelihood ratio method using an integrated luminosity of 1.3 fb^{-1} [9]; and a limit of 5.1×10^{-8} using a Bayesian neural network and an integrated luminosity of 6.1 fb^{-1} [10]. The result presented here uses the full D0 dataset corresponding to 10.4 fb^{-1} of $p\bar{p}$ collisions and supersedes our previous results.

Recently, the LHCb Collaboration has presented the first evidence for this decay, at a branching fraction consistent with the SM prediction [11]. Previous to this result, the most stringent 95% C.L. limits on this decay came from the LHCb [12], CMS [13], and ATLAS [14] Collaborations, which quote limits of $\mathcal{B}(B_s^0 \rightarrow \mu^+\mu^-) < 4.5 \times 10^{-9}$, 7.7×10^{-9} , and 22×10^{-9} , respectively. The CDF Collaboration sees an excess over background corresponding to a branching fraction of $(18_{-9}^{+11}) \times 10^{-9}$ and to a 95% C.L. upper limit of 40×10^{-9} [15].

II. THE D0 DETECTOR

The D0 experiment collected data at the Fermilab Tevatron $p\bar{p}$ Collider at $\sqrt{s}=1.96$ TeV from 2001 through the shutdown of the Tevatron in 2011, a period referred to as Run II.

The D0 detector is described in detail elsewhere [16]. For the purposes of this analysis, the most important parts of the detector are the central tracker and the muon system. The inner region of the D0 central tracker consists of a silicon microstrip tracker (SMT) that covers pseudorapidities $|\eta| < 3$ [17]. In the spring of 2006, an additional layer of silicon (Layer 0) was added close to the beam pipe [18]. Since the detector configuration changed significantly with this addition, the D0 dataset is divided into two distinct periods (Run IIa and Run IIb), with the analysis performed separately for each period. Moving away from the interaction region, the next detector subsystem encountered is the D0 central fiber tracker (CFT), which consists of 16 concentric cylinders of scintillating fibers, covering $|\eta| < 2.5$. Both the SMT and CFT are located within a 2 T superconducting solenoidal magnet. The D0 muon system is located outside of the finely segmented liquid argon sampling calorimeter. The muon system consists of three layers of tracking detectors and trigger scintillators, one layer in front of 1.8 T toroidal magnets and two additional layers after the toroids. The muon system covers $|\eta| < 2$.

The data used in this analysis were collected with a suite of single muon and dimuon triggers.

III. ANALYSIS OVERVIEW

This analysis was performed with the relevant dimuon mass region blinded until all analysis procedures were final. Our dimuon mass resolution is not sufficient to separate $B_s^0 \rightarrow \mu^+\mu^-$ from $B_d^0 \rightarrow \mu^+\mu^-$, but in this analysis we assume that there is no contribution from $B_d^0 \rightarrow \mu^+\mu^-$, since this decay is expected to be suppressed with respect to $B_s^0 \rightarrow \mu^+\mu^-$ by the ratio of the CKM matrix elements $|V_{td}/V_{ts}|^2 \approx 0.04$ [19]. The most stringent 95% C.L. limit on the decay $B_d^0 \rightarrow \mu^+\mu^-$, which is from the LHCb experiment [11], is $\mathcal{B}(B_d^0 \rightarrow \mu^+\mu^-) < 9.4 \times 10^{-10}$.

$B_s^0 \rightarrow \mu^+\mu^-$ candidates are identified by selecting two high-quality muons of opposite charge that form a good three-dimensional vertex well-separated from the primary $p\bar{p}$ interaction due to the relatively long lifetime of the B_s^0 meson [19]. A crucial requirement for this analysis is the suppression of the large dimuon background arising from semileptonic b and c quark decays. Figure 2 shows a schematic diagram of the signal decay and the two dominant background processes. Backgrounds in the dimuon effective mass region below the B_s^0 mass are dominated by sequential decays such as $b \rightarrow \mu^-\nu c$ with $c \rightarrow \mu^+\nu X$, as shown in Fig. 2(b). Backgrounds in the dimuon mass region above the B_s^0 mass are dominated by double semileptonic decays such as $b(\bar{c}) \rightarrow \mu^-\nu X$ and $\bar{b}(c) \rightarrow \mu^+\nu X$, as shown in Fig. 2(c). For both of these backgrounds, the muons do not form a real vertex, but the tracks can occasionally be close enough in space to be reconstructed as a “fake” vertex.

Figure 2 illustrates the differences between signal and background that we exploit as a general analysis strategy. The dimuon system itself should form a good vertex consistent with the decay of a single particle originating from the $p\bar{p}$ interaction vertex. The B_s^0 candidate should have a small impact parameter with respect to the primary $p\bar{p}$ interaction vertex, while the individual muons should in general have fairly large impact parameters. In addition to quantities related to the dimuon system, Fig. 2 illustrates that the environment surrounding the B_s^0 candidate should be quite different for signal compared to backgrounds. The dimuon system for the signal should be fairly well isolated, while the fake dimuon vertex in background events is likely to have additional tracks and additional vertices nearby. No single variable is able to provide definitive discrimination against these backgrounds, so we use a multivariate technique as described in Sec. VII to exploit these differences between signal and background.

In addition to dimuon backgrounds from semileptonic heavy quark decays, there are peaking backgrounds arising from $B_s^0 \rightarrow hh$ or $B_d^0 \rightarrow hh$ where hh can be KK , $K\pi$ or $\pi\pi$. Of these, $B_s^0 \rightarrow KK$ is the dominant contribution. The K or π mesons can be misidentified as a muon by decay in flight $K/\pi \rightarrow \mu\nu$ or by penetrating far enough in the detector to create hits in the muon system. For these decays to be misidentified as signal, both hadrons must be misidentified as a muon, but since the decay we are looking for is rare, $B_s^0/B_d^0 \rightarrow hh$ decays constitute a background of magnitude similar to that of the expected signal.

The number of $B_s^0 \rightarrow \mu^+\mu^-$ decays expected in our dataset is determined from analysis of the normalization decay channel $B^\pm \rightarrow J/\psi K^\pm$, with $J/\psi \rightarrow \mu^+\mu^-$, as described in detail in Sec. VI.

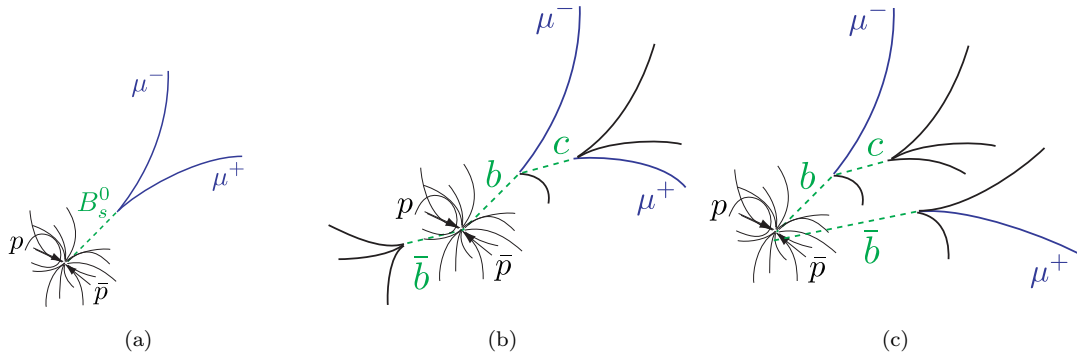


FIG. 2: (color online) Schematic diagrams showing (a) the signal decay, $B_s^0 \rightarrow \mu^+ \mu^-$, and main backgrounds: (b) sequential decay, $b \rightarrow c \mu^-$ followed by $c \rightarrow \mu^+$, and (c) double semileptonic decay, $b \rightarrow \mu^-$ and $\bar{b} \rightarrow \mu^+$.

IV. MONTE CARLO SIMULATION

Detailed Monte Carlo (MC) simulations for both the $B_s^0 \rightarrow \mu^+ \mu^-$ signal and the $B^\pm \rightarrow J/\psi K^\pm$ normalization channels are obtained using the PYTHIA [20] event generator, interfaced with the EVTGEN [21] decay package. The MC includes primary production of $b\bar{b}$ quarks that are approximately back-to-back in azimuthal angle, and also includes gluon splitting $g \rightarrow b\bar{b}$ where the gluon may have radiated from any quark in the event. The latter leads to a relatively collimated $b\bar{b}$ system that produces the dominant background when both b and \bar{b} quarks decay semileptonically to muons.

The detector response is simulated using GEANT [22] and overlaid with events from randomly collected $p\bar{p}$ bunch crossings to simulate multiple $p\bar{p}$ interactions. A correction to the MC width of the dimuon mass distribution is determined from $J/\psi \rightarrow \mu^+ \mu^-$ decays in data, and this correction is then scaled to the B_s^0 mass region. The $B_s^0 \rightarrow \mu^+ \mu^-$ mass distribution in the MC is well described by a double Gaussian function with the two means constrained to be equal, but with the widths (σ_1 and σ_2) and relative fractions determined by a fit to the corrected mass distribution. The average width is $\sigma_{av} = f\sigma_1 + (1-f)\sigma_2 = 125$ MeV, where f is the fraction of the area associated with σ_1 .

We measure the trigger efficiencies in the data using events with no requirements other than a $p\bar{p}$ bunch crossing (zero-bias events) or events requiring only an inelastic $p\bar{p}$ interaction (minimum-bias events). The MC generation does not include trigger efficiencies, but the MC events are reweighted to reproduce the trigger efficiency as a function of the muon transverse momentum (p_T). In addition, the MC events are corrected to describe the p_T distribution of B mesons above the trigger threshold, as determined from $B^\pm \rightarrow J/\psi K^\pm$ decays. Since the trigger conditions changed throughout the course of Run II, the p_T corrections are determined separately for five different data epochs, with each epoch typically separated by an accelerator shut-down of a few months' duration. Fig-

ure 3 compares data and MC for several p_T distributions in the normalization channel, after these corrections. The background components in the B^\pm distributions are removed by a side-band subtraction technique, that is, by subtracting the corresponding distributions from events above and below the B^\pm mass region. As can be seen in Fig. 3, the p_T distributions in the MC simulation and normalization channel data are generally in excellent agreement. Figure 3 shows a single data epoch, but all data epochs show similar agreement.

In addition to the signal MC, we also study the $B_s^0 \rightarrow KK$ background using a sample of MC events that contains about six times the expected number of such events in our data sample.

V. EVENT SELECTION

The B_s^0 candidate events selected for further study are chosen as follows. We select two high-quality, oppositely-charged muons based on information from both the central tracker and the muon detectors. The primary vertex (PV) of each $p\bar{p}$ interaction is defined using all available well-reconstructed tracks and constrained by the mean beam-spot position in the transverse plane. If a bunch crossing has more than one $p\bar{p}$ interaction vertex, we ensure that both muons are consistent with originating from the same PV. Tracks reconstructed in the central tracker are required to have at least two hits in both the SMT and CFT detectors. These tracks are extrapolated to the muon system, where they are required to match hits observed in the muon detectors. Each muon is required to have transverse momentum $p_T > 1.5$ GeV and to have pseudorapidity $|\eta| < 2$. Both muons are required to have hits in the muon detectors in front of the toroids, and at least one of the muons must also have hits in at least one of the muon layers beyond the toroids. To reduce combinatorial backgrounds, the two muons must form a three-dimensional vertex with $\chi^2/dof < 14$. The dimuon vertex is required to be well separated from the PV by

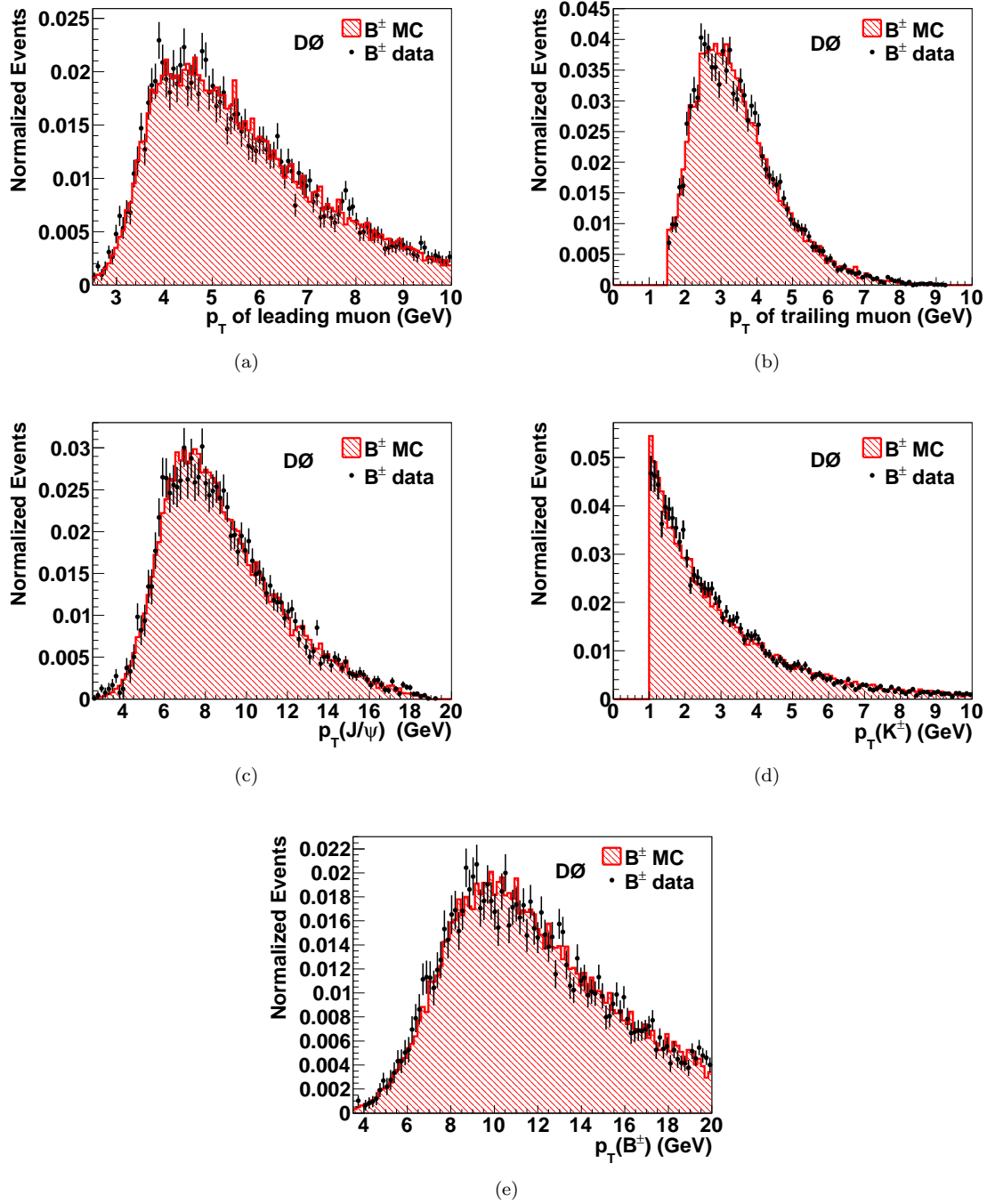


FIG. 3: (color online) Comparison of p_T distributions for data and MC simulation, for the normalization channel $B^\pm \rightarrow J/\psi K^\pm$, in a single data epoch, (a) for the higher- p_T (leading) muon, (b) lower- p_T (trailing) muon, (c) J/ψ , (d) kaon, and (e) B^\pm meson. All distributions are normalized to unit area.

examining the transverse decay length. The transverse decay length L_T is defined as $L_T = \vec{l}_T \cdot \vec{p}_T / |\vec{p}_T|$, where the vector \vec{l}_T is from the PV to the dimuon vertex in the transverse plane, and \vec{p}_T is the transverse momentum vector of the dimuon system. The quantity σ_{L_T} is the uncertainty on the transverse decay length determined from

track parameter uncertainties and the uncertainty in the position of the PV. To reduce prompt backgrounds, the transverse decay length significance of the dimuon vertex, L_T/σ_{L_T} , must be greater than three. Events are selected for further study if the dimuon mass $M_{\mu\mu}$ is between 4.0 GeV and 7.0 GeV. These criteria are intended

to be fairly loose to maintain high signal efficiency, with further discrimination provided by the multivariate technique discussed in Sec. VII.

The normalization channel decays $B^\pm \rightarrow J/\psi K^\pm$ with $J/\psi \rightarrow \mu^+\mu^-$ are reconstructed in the data by first finding the decay $J/\psi \rightarrow \mu^+\mu^-$ and then adding a third track, assumed to be a charged kaon, to the dimuon vertex. The selection criteria for the signal and normalization channel are kept as similar as possible. In addition to the above requirements on the muons, we require the K^\pm to have $p_T > 1$ GeV and $|\eta| < 2$, and we require the three-track vertex to have $\chi^2/dof < 6.7$. In the normalization channel the dimuon mass is required to be in the J/ψ mass region, $2.7 \text{ GeV} < M(\mu^+\mu^-) < 3.45 \text{ GeV}$.

VI. DETERMINATION OF THE SINGLE EVENT SENSITIVITY

To determine the number of $B_s^0 \rightarrow \mu^+\mu^-$ decays we expect in the data, we normalize to the number of $B^\pm \rightarrow J/\psi K^\pm$ candidates observed in the data. The number of $B^\pm \rightarrow J/\psi K^\pm$ decays is used to determine the single event sensitivity (SES), defined as the branching fraction for which one event is expected to be present in the dataset. The SES is calculated from

$$\text{SES} = \frac{1}{N(B^\pm)} \times \frac{\epsilon(B^\pm)}{\epsilon(B_s^0)} \frac{f(b \rightarrow B^\pm)}{f(b \rightarrow B_s^0)} \times \mathcal{B}(B^\pm \rightarrow J/\psi K^\pm) \times \mathcal{B}(J/\psi \rightarrow \mu^+\mu^-).$$

In this expression $N(B^\pm)$ is the number of $B^\pm \rightarrow J/\psi K^\pm$ decays observed in the data, as discussed below. The efficiency for reconstructing the normalization channel decay, $\epsilon(B^\pm)$, and the signal channel, $\epsilon(B_s^0)$, are determined from MC simulations as discussed in more detail below. The fragmentation ratio $f(b \rightarrow B^\pm)/f(b \rightarrow B_s^0)$ is the relative probability of a b quark fragmenting to a B^\pm compared to a B_s^0 . We use the “high energy” average $f(b \rightarrow B_s^0)/f(b \rightarrow B^\pm) = 0.263 \pm 0.017$ provided by the Heavy Flavor Averaging Group [23] for the 2012 Particle Data Group compilation [19], which is consistent with other recent measurements [24]. The product of the branching fractions $\mathcal{B}(B^\pm \rightarrow J/\psi K^\pm) \times \mathcal{B}(J/\psi \rightarrow \mu^+\mu^-)$ is $(6.01 \pm 0.21) \times 10^{-5}$ [19].

Figure 4 shows the normalization channel mass distribution, $M(\mu^+\mu^-K)$, for the entire Run II dataset. The mass distribution is fitted to a double Gaussian function to model the normalization channel decay and an exponential function to model the dominant background. A hyperbolic tangent threshold function is also included in the fit to model partially reconstructed B meson decays, primarily $B_d^0 \rightarrow J/\psi K^{0*}$. A possible contribution from $B^\pm \rightarrow J/\psi \pi^\pm$ is also included in the fit, although this contribution is not statistically significant and is not shown in the Fig. 4. Systematic uncertainties on $N(B^\pm)$ are determined from variations in the mass range of the fit, the histogram binning, and the background model. An additional systematic uncertainty on $N(B^\pm)$ is due

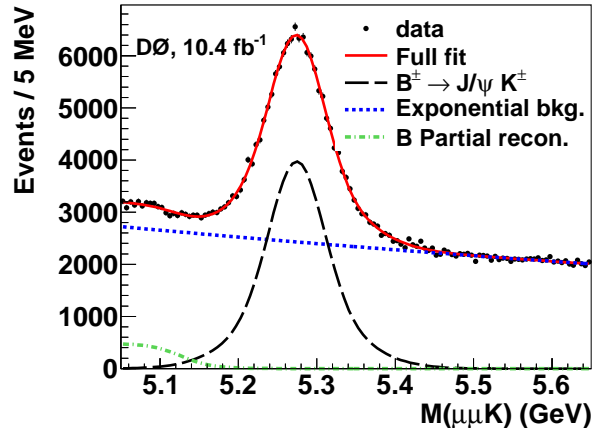


FIG. 4: (color online) Invariant mass distribution for the normalization channel $B^\pm \rightarrow J/\psi K^\pm$ for the entire Run II dataset. The full fit is shown as the solid line, the $B^\pm \rightarrow J/\psi K^\pm$ contribution is shown as the dashed line, the exponential background is shown as the dotted line, and the contribution from partially reconstructed B meson decays is shown as the dot-dash line.

to the candidate selection. If an event has more than one $B^\pm \rightarrow J/\psi K^\pm$ candidate, we retain only the candidate with the best vertex χ^2 . This choice results in fewer overall reconstructed $B^\pm \rightarrow J/\psi K^\pm$ decays but also less background. To determine the systematic effect due to this choice, we have reconstructed $B^\pm \rightarrow J/\psi K^\pm$ decays in two of the five data epochs retaining all candidates. The SES depends on the ratio $N(B^\pm)/\epsilon(B^\pm)$, and we find that this ratio varies at most 2.2%, which we take as an additional systematic uncertainty on $N(B^\pm)$. We observe a total of $(87.4 \pm 3.0) \times 10^3$ $B^\pm \rightarrow J/\psi K^\pm$ decays in the full dataset, where the uncertainty includes both statistical and systematic effects.

The ratio of reconstruction efficiencies that enters into the SES is determined from MC simulation. One source of systematic uncertainty in the efficiency ratio arises from the trigger efficiency corrections applied to the MC, as described in Sec. IV. The variation in these corrections over data epochs with similar trigger conditions allows us to set a 1.5% systematic uncertainty on the efficiency ratio due to this source. An additional systematic uncertainty arises from the efficiency for finding a third track. There could be a data/MC discrepancy in this efficiency which will not cancel in the ratio. We evaluate this systematic uncertainty by comparing the efficiency for finding an extra track in data and MC in the four-track decay $B_d^0 \rightarrow J/\psi K^{0*}$ with $K^{0*} \rightarrow K\pi$ and in the three-track normalization channel decay $B^\pm \rightarrow J/\psi K^\pm$. From this study, we determine that the data/MC efficiency ratio for identifying the third track varies with data epoch but is on average 0.88 ± 0.06 , where the uncertainty includes statistical uncertainties from the fits

used to extract the number of signal events, and systematic uncertainties estimated from fit variations. The efficiency for B^\pm reconstruction is adjusted in each data epoch for this track-finding efficiency correction. The reconstruction efficiency ratio $\epsilon(B^\pm)/\epsilon(B_s^0)$ is determined to be $(13.0 \pm 0.5)\%$ on average, but varies over the different data epochs by about 1.0%. The efficiency for the $B^\pm \rightarrow J/\psi K^\pm$ decay is impacted by the softer p_T distribution of the muons in the three-body decay as well as the fairly hard ($p_T > 1$ GeV) cut on the p_T of the kaon, and the candidate selection which retains only the three-track candidate with the best vertex χ^2 .

When all statistical and systematic uncertainties are taken into account, the SES is found to be $(0.336 \pm 0.029) \times 10^{-9}$ before the multivariate selection, yielding a SM expected number of $B_s^0 \rightarrow \mu^+ \mu^-$ events of 10.4 ± 1.1 events in our data sample.

VII. MULTIVARIATE DISCRIMINANT

A boosted decision tree (BDT) algorithm, as implemented in the TMVA package of ROOT [25], is used to differentiate between signal and the dominant backgrounds. The BDT is trained using MC simulation for the signal and data sidebands for the background. The data sidebands include events in the dimuon mass range 4.0–4.9 GeV (low-mass sidebands) and 5.8–7.0 GeV (high-mass sidebands), with all selection cuts applied. The low-mass sidebands are dominated by sequential decays, illustrated in Fig. 2(b), while the the high-mass sidebands are dominated by double B hadron decays, as illustrated in Fig. 2(c). We therefore train two BDTs to separately discriminate against these two backgrounds. Each BDT discriminant uses 30 variables that fall into two general classes.

One class of variables includes kinematic and topological quantities related to the dimuon system. These variables include the pointing angle, defined as the angle between the dimuon momentum vector $\vec{p}(\mu^+ \mu^-)$ and the vector from the PV to the dimuon vertex. The dimuon p_T and impact parameter, as well as the p_T values of the individual muons and their impact parameters, are also used as discriminating variables. As examples of dimuon system variables that discriminate between signal and background, Fig. 5(a) shows the impact parameter significance (impact parameter divided by its uncertainty) of the B_s^0 candidate for signal MC and background, and Fig. 5(b) shows the minimum impact parameter significance for the individual muons, that is, the smaller of the two values.

A second general class of variables used in the BDT discriminants includes various isolation-related quantities. Isolation is defined with respect to a momentum vector \vec{p} by constructing a cone in azimuthal angle ϕ and pseudorapidity η around the momentum vector, with the cone radius defined by $\mathcal{R} = \sqrt{\Delta\eta^2 + \Delta\phi^2}$. The isolation \mathcal{I} is then defined as $\mathcal{I} = p_T/[p_T + p_T(\text{cone})]$ where $p_T(\text{cone})$

is the scalar sum of the p_T of all tracks (excluding the track of interest) with \mathcal{R} less than some cut-off value, chosen to be $\mathcal{R} = 1$ in this analysis. For a perfectly isolated track (that is, no other tracks in the cone), $\mathcal{I} = 1$. Figure 2 shows that background events are expected to be less isolated than signal events. For maximum signal/background discrimination, we define isolation cones around the dimuon direction and around each muon individually. From simulation studies, we find that for background events, the two muons are often fairly well separated in space, so using individual isolation cones around each muon adds discriminating power. Figure 6 compares signal MC and data sidebands for two examples of isolation variables.

We also search for additional vertices near the dimuon vertex using two different techniques. As illustrated by Fig. 2, in background events the muons often form a good vertex with another charged track. We try to reconstruct such vertices using tracks that are associated with the same PV as the dimuon pair, which have an impact parameter with respect to the PV of at least 30 microns, and which have an impact parameter significance of at least 3.0. If a track satisfying these requirements forms a vertex with one of the muons with a vertex $\chi^2/dof < 5.0$, we consider this an additional vertex. Additional tracks, satisfying the same requirements as above, can be included in this vertex if they do not increase the vertex χ^2 by more than 5.0. This procedure is carried out with both muons, allowing for the possibility of finding an additional vertex with either or both of the muons. We also attempt to reconstruct additional vertices using tracks that have an impact parameter significance with respect to the dimuon vertex of less than 4.0. We allow these vertices to include or not include one of the muons. When an additional vertex is successfully reconstructed, the vertex χ^2 , the invariant mass of the particles included in the vertex, and the vertex pointing angle are used as discriminating variables in the BDTs. In the case where no such vertices are found, these variables are set to nonphysical values. We find that, for the background sidebands, at least one additional vertex is reconstructed 80% of the time, while for the signal MC, one or more additional vertices are found 40% of the time.

To verify that the MC simulation is a good representation of the data, we compare the sideband-subtracted normalization channel data with the normalization channel MC. Figure 7 compares the normalization channel data and the MC simulation for the B^\pm meson impact parameter significance and the minimum muon impact parameter significance. Figure 8 shows the same comparison for the dimuon and individual muon isolation variables. We check all 30 variables used in the multivariate discriminant to confirm good agreement between data and MC for the normalization channel.

We make additional requirements on both the data sidebands and the signal MC before events are used in the BDT training. These requirements include dimuon $p_T > 5$ GeV and the cosine of the dimuon pointing angle

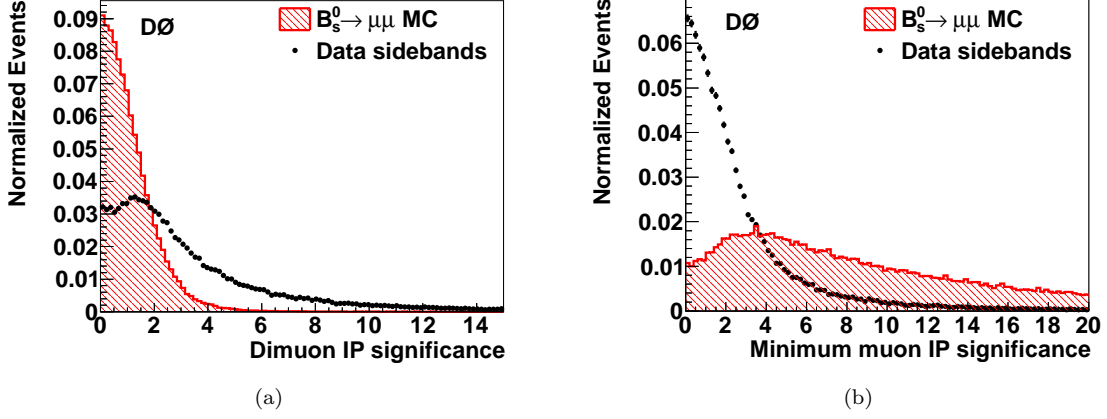


FIG. 5: (color online) Comparison of signal MC and background sideband data for (a) the B_s^0 candidate impact parameter significance and (b) the minimum muon impact parameter significance. All distributions are normalized to unit area.

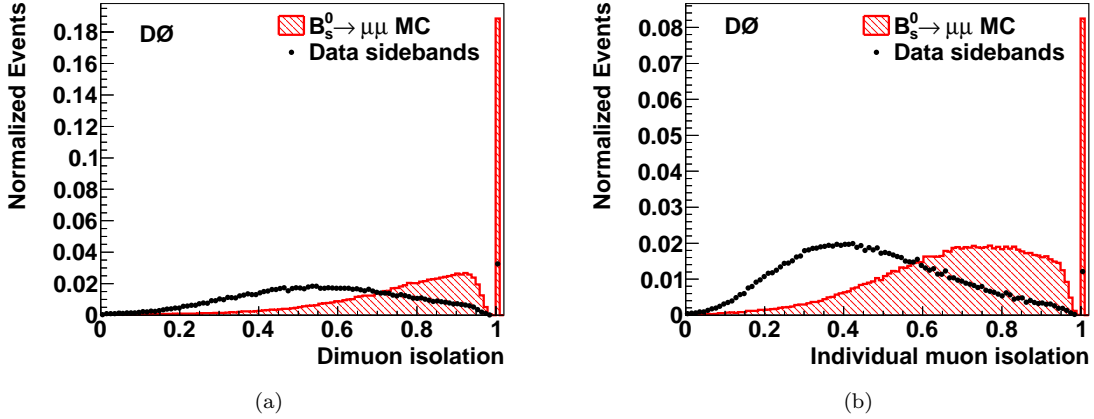


FIG. 6: (color online) Comparison of signal MC and background sideband data for (a) isolation defined with respect to the dimuon system and (b) for the average of the two isolations defined with respect to the individual muons. All distributions are normalized to unit area.

> 0.95 . These requirements are 78% efficient on average in retaining signal events but exclude about 96% of the background. We find a significant enhancement in background rejection from the BDT discriminants using these additional requirements before BDT training. These requirements are $(93 \pm 1)\%$ efficient for the normalization mode MC, and $(91 \pm 3)\%$ efficient for the normalization mode data.

To improve the statistics available for training, the data epochs are combined and used together to train the BDT. The signal MC samples for each data epoch are combined according to the integrated luminosity for each epoch into a common sample. The data sidebands and signal MC are then randomly split into three samples. Sample A, with 25% of the events, is used to train the BDTs. Sample B, with 25% of the events, is used to optimize the selections on the BDT response. Sample C, with

50% of the events, is used to determine the expected signal (from the MC sample) and background (from the data sideband sample) yields. The results of the TMVA BDT training for both BDT1, trained to remove sequential decay backgrounds, and BDT2, trained to remove double semileptonic B meson decays, can be seen in Fig. 9. We check that the response of both BDT discriminants is independent of dimuon mass over the relevant mass range. The optimal BDT selections are determined by optimizing the expected limit on $\mathcal{B}(B_s^0 \rightarrow \mu^+ \mu^-)$ and are found to be $\text{BDT1} > 0.19$ and $\text{BDT2} > 0.26$.

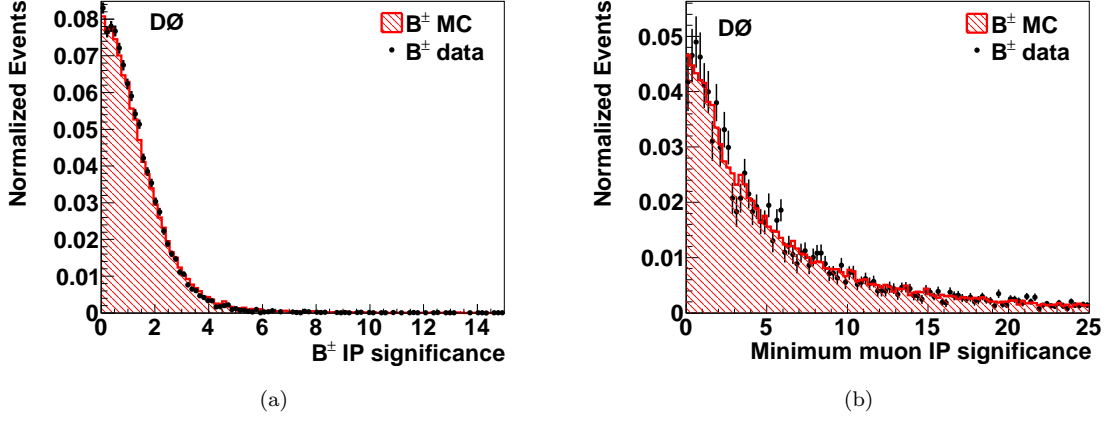


FIG. 7: (color online) Comparison of normalization channel MC and sideband-subtracted data for (a) B^\pm impact parameter significance and (b) the minimum muon impact parameter significance. All distributions are normalized to unit area.

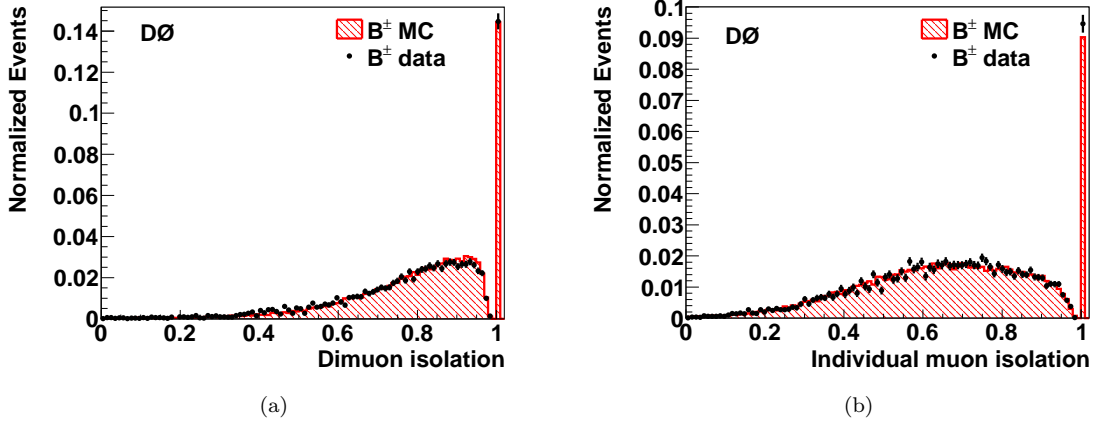


FIG. 8: (color online) Comparison of normalization channel MC and sideband-subtracted data for (a) dimuon isolation and (b) the average of the two individual muon isolations. All distributions are normalized to unit area.

VIII. BACKGROUND ESTIMATES AND EXPECTED LIMIT

Figure 10 shows the blinded dimuon mass distributions before (Fig. 10(a)) and after (Fig. 10(b)) the BDT selection cuts for the half of the data (sample C) used to estimate the number of background events. The signal window within the blinded region is chosen to maximize the signal significance $S/\sqrt{S+B}$, where S is the expected number of signal events as determined from the SM branching fraction, and B is the expected background. The number of expected background events is determined by a likelihood fit to the data in the sideband regions, which is then interpolated into the blinded region. The optimum signal region is determined to be $\pm 1.6\sigma$ centered on the B_s^0 mass, where $\sigma = 125$ MeV is the average width of the double Gaussian used to fit

the dimuon mass distribution in the $B_s^0 \rightarrow \mu^+\mu^-$ MC sample. The blinded region includes a control region of width 2σ on each side of the signal window. While only half of the dataset is shown, the numbers of expected background events quoted in Fig. 10 are scaled to the full dataset. The numbers given are for the estimated dimuon background events in the signal region.

The efficiency for retaining signal events when all BDT selections are applied, including the pre-training cuts (see Sec. VII) and the final BDT cuts, is determined to be 0.12 ± 0.01 , where the error is due to variation over the different data epochs. We obtain a final SES of $(2.8 \pm 0.24) \times 10^{-9}$, corresponding to an expected number of signal events at the SM branching fraction of 1.23 ± 0.13 . For the dimuon background the expected number of events in the signal and control regions is determined by applying a log likelihood fit to the dimuon mass dis-

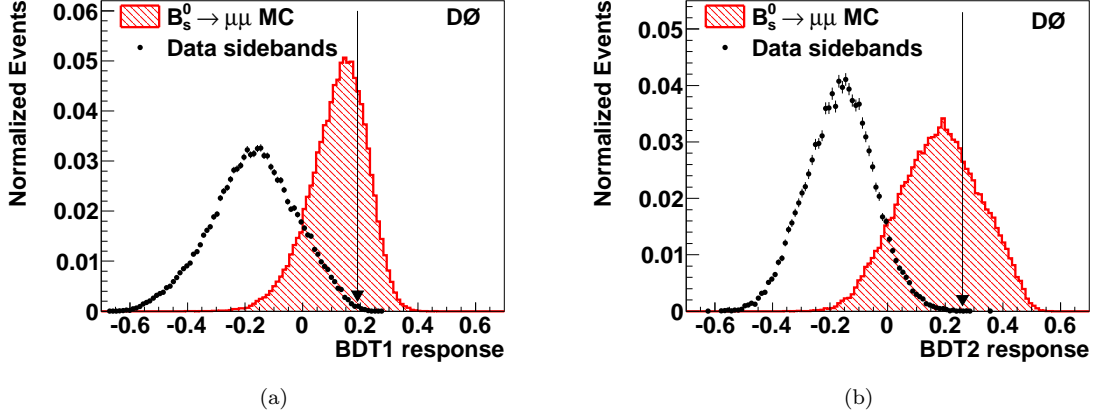


FIG. 9: (color online) Distributions of the BDT response for (a) BDT1, trained against sequential decay backgrounds, and (b) BDT2, trained against double B decay backgrounds. MC simulation is used for the signal, while the data sidebands are used for the backgrounds. The vertical lines denote the BDT selection cuts in the analysis. All distributions are normalized to unit area.

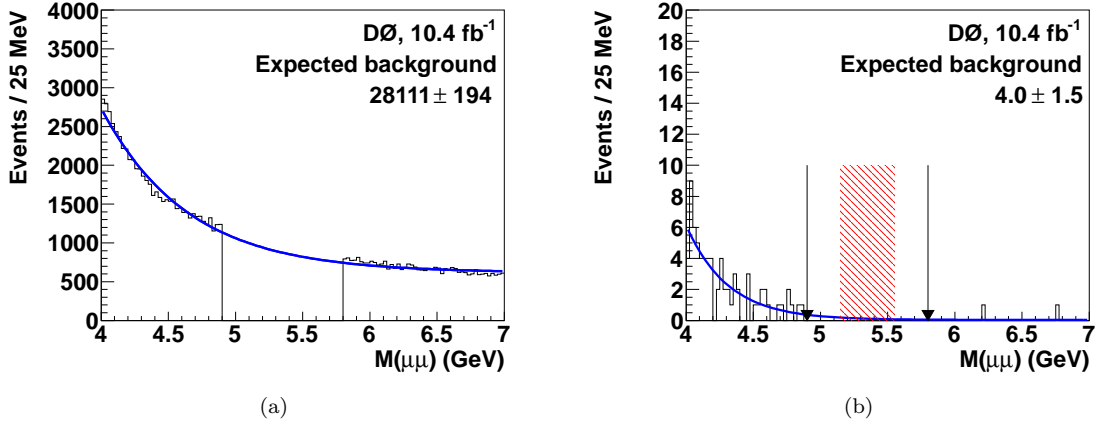


FIG. 10: (color online) Dimuon mass distribution for sample C (a) before and (b) after BDT selection cuts. The edges of the blinded region are denoted in (b) by the vertical lines at 4.9 and 5.8 GeV, and the shaded area denotes the signal window. The curves are fits to an exponential plus constant function. The numbers of expected background events are determined from an interpolation of the fit into the signal window and scaled to the full dataset.

tribution using an exponential plus constant functional form. The fit is performed excluding the blinded region, and the resulting fit is interpolated into the signal and control regions. This procedure yields an expected number of dimuon background events in the signal region of 4.0 ± 1.5 events, where the uncertainty is only statistical. The corresponding estimate for the expected number of events in the control region is 6.7 ± 2.6 events, with 5.3 ± 1.9 events expected in the lower control region (dimuon masses from 4.9 to 5.15 GeV), and 1.4 ± 1.4 events in the upper control region (dimuon masses from 5.55 to 5.8 GeV). To determine the systematic uncertainty on the background estimate, we use other functional forms for the background fit, resulting in a sys-

tematic uncertainty of 0.6 events. Adding the statistical and systematic errors in quadrature yields a final dimuon background estimate in the signal region of 4.0 ± 1.6 events and 6.7 ± 2.7 events in the control region.

In addition to the dimuon background, there is background from the decay mode $B_s^0 \rightarrow K^+ K^-$, which has kinematics very similar to the signal. We estimate this background by scaling the expected number of signal events by the appropriate branching fractions [19] and by the ratio of the probabilities for both K mesons to be misidentified as muons, $\epsilon(KK \rightarrow \mu\mu)$, to the probability that two muons are correctly identified as muons, $\epsilon(\mu\mu \rightarrow \mu\mu)$. The probability that a K meson is misidentified as a muon is measured in the data using $D^0 \rightarrow K\pi$

decays. We assume that the probability of two K mesons being misidentified as muons is the product of the probabilities for each individual K meson. The muon identification efficiency is measured in the data from $J/\psi \rightarrow \mu\mu$ decays. The efficiency ratio $\epsilon(KK \rightarrow \mu\mu)/\epsilon(\mu\mu \rightarrow \mu\mu)$ is determined to be $(3.0 \pm 1.1) \times 10^{-5}$. We estimate the background from $B_s^0 \rightarrow KK$ decays to be 0.28 ± 0.11 events. We also find a consistent estimate of this background using a $B_s^0 \rightarrow KK$ MC sample. Other possible peaking backgrounds such as $B_d^0 \rightarrow K\pi$ and $B_s^0 \rightarrow K\pi$ are negligible due to the combination of smaller branching fractions and a $\pi \rightarrow \mu$ misidentification probability that is more than a factor of 10 smaller than the $K \rightarrow \mu$ misidentification probability in the D0 detector.

We set an upper limit on the $B_s^0 \rightarrow \mu^+\mu^-$ branching fraction using the CL_s, or modified frequentist method [26]. A Poisson likelihood function is used to calculate the number of signal events which would occur with a probability of 0.05 (for a 95% CL upper confidence limit) when N_{obs} data events are observed in the signal region with a known expected number of background events.

The limit calculation includes a convolution over probability distributions representing the uncertainties in the background and the signal. The uncertainty in the $B_s^0 \rightarrow KK$ peaking background is assumed to be Gaussian. The dimuon background in the signal region is estimated by the fit shown in Fig. 10(b). The normalized likelihood function from this fit is used as the probability distribution function for the dimuon background in the convolution. The expected number of signal events, assuming the SM branching fraction, is 1.23 ± 0.13 events, with the uncertainty assumed to be Gaussian. The total expected background is 4.3 ± 1.6 events. Weighting each possible outcome by its Poisson probability yields an expected 95% C.L. upper limit on the branching fraction $\mathcal{B}(B_s^0 \rightarrow \mu^+\mu^-)$ of 23×10^{-9} .

Upon unblinding, a total of nine events is found in the control region above and below the signal region, as shown in Fig. 11. Six events are found in the control region below the signal window, and three events are found in the control region above the signal window. This number of events and their distribution within the control regions is in agreement with the expected number of background events interpolated from the data sidebands. As seen in Fig. 11, three events are found in the dimuon mass signal window, in agreement with the expected background and also with the expected signal + background. We check that the properties of all events found in the blinded region, such as the p_T of the dimuon system, the p_T of the individual muons, the dimuon pointing angle, and the various isolation quantities, are consistent with expectations. We also check that, as the BDT cuts are relaxed, the number of events observed in the signal region remains in good agreement with expectations, as shown in Fig. 12.

The observed number of events and the SES allow us to set a 95% C.L. upper limit $\mathcal{B}(B_s^0 \rightarrow \mu^+\mu^-) < 15 \times 10^{-9}$.

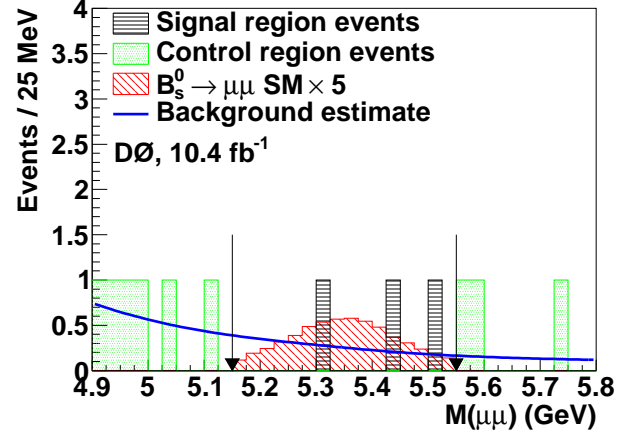


FIG. 11: (color online) Dimuon mass distribution in the blinded region for the full dataset after BDT selections are applied. The curve shows the fit from Fig. 10(b) used to determine the expected number of background events. The SM expectation for signal events multiplied by five is also indicated. The vertical lines mark the edge of the signal window.

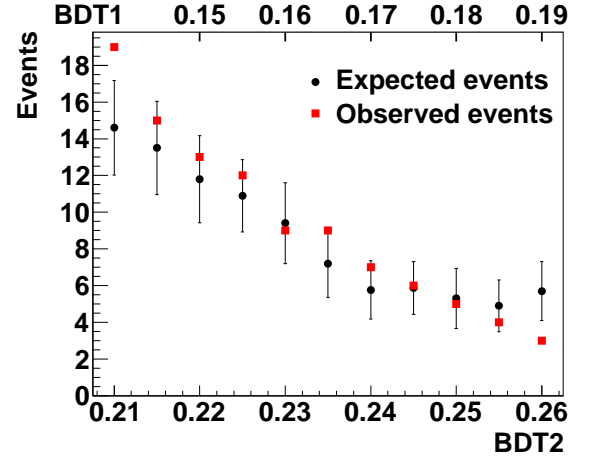


FIG. 12: (color online) Expected number of events and observed number of events in the signal region as the two BDT cuts are relaxed in parallel. The expected number of events includes the dimuon background, the $B_s^0 \rightarrow KK$ background, and the expected number of signal events. The upper horizontal axis shows the cut applied to BDT1, while the lower horizontal axis shows the cut applied to BDT2.

IX. SUMMARY

In summary, we have searched for the rare decay $B_s^0 \rightarrow \mu^+\mu^-$ in the full D0 dataset. We employ two Boosted Decision Tree multivariate discriminators, one trained to discriminate against sequential decays $b(\bar{b}) \rightarrow c\mu^-(\bar{c}\mu^+)X$ followed by $c(\bar{c}) \rightarrow \mu^+(\mu^-)X$ and the other

to discriminate against double semileptonic decays $b \rightarrow \mu^- X$ and $\bar{b} \rightarrow \mu^+ X$. The sidebands around the signal region in the dimuon invariant mass distribution are used to estimate the dominant backgrounds. The expected limit is 23×10^{-9} , and the expected background (signal) in the signal region is 4.3 ± 1.6 (1.23 ± 0.13) events. We observe three events in the signal region consistent with expected background. The probability that the background alone (signal + background) could produce the observed number of events or a larger number of events in the signal region is 0.77 (0.88). We set an observed 95% C.L. upper limit $\mathcal{B}(B_s^0 \rightarrow \mu^+ \mu^-) < 15 \times 10^{-9}$. This upper limit supersedes the previous D0 95% C.L. limit of 51×10^{-9} [10], and improves upon that limit by a factor of 3.4. The improvement in the expected limit is a factor of 1.7 greater than the improvement that would be expected due to increased luminosity alone. The additional improvement arises from the inclusion of several

isolation-type variables in the multivariate discriminants and in the use of two separate discriminants to distinguish backgrounds from sequential b quark decays and double b quark decays. This result is the most stringent Tevatron limit and is compatible with the recent evidence of this decay produced by the LHCb experiment [11].

We thank the staffs at Fermilab and collaborating institutions, and acknowledge support from the DOE and NSF (USA); CEA and CNRS/IN2P3 (France); MON, NRC KI and RFBR (Russia); CNPq, FAPERJ, FAPESP and FUNDUNESP (Brazil); DAE and DST (India); Colciencias (Colombia); CONACyT (Mexico); NRF (Korea); FOM (The Netherlands); STFC and the Royal Society (United Kingdom); MSMT and GACR (Czech Republic); BMBF and DFG (Germany); SFI (Ireland); The Swedish Research Council (Sweden); and CAS and CNSF (China).

-
- [1] K. De Bruyn *et al.*, Phys. Rev. Lett. **109**, 041801 (2012).
 - [2] A. J. Buras *et al.*, Eur. Phys. J. **C72**, 2172 (2012).
 - [3] A. J. Buras, Acta. Phys. Polon. B **41**, 2487 (2010).
 - [4] S. R. Choudhury and N. Gaur, Phys. Lett. B **451**, 86 (1999).
 - [5] J. K. Parry, Nucl. Phys. **B760**, 38 (2007).
 - [6] R. L. Arnowitt, B. Dutta, T. Kamon and M. Tanaka, Phys. Lett. B **538**, 121 (2002).
 - [7] J. R. Ellis, J. S. Lee, and A. Pilaftsis, Phys. Rev. D **76**, 115011 (2007).
 - [8] V. Abazov *et al.* (D0 Collaboration), Phys. Rev. Lett. **94**, 071802 (2005).
 - [9] V. Abazov *et al.* (D0 Collaboration), Phys. Rev. D **76**, 092001 (2007).
 - [10] V. M. Abazov *et al.* (D0 Collaboration), Phys. Lett. B **693**, 534 (2010).
 - [11] R. Aaij *et al.* (LHCb Collaboration), Phys. Rev. Lett. **110**, 021801 (2013).
 - [12] R. Aaij *et al.* (LHCb Collaboration), Phys. Rev. Lett. **108**, 231801 (2012).
 - [13] S. Chatrchyan *et al.* (CMS Collaboration), J. High Energy Phys. **04**, 033 (2012).
 - [14] G. Aad *et al.* (ATLAS Collaboration), Phys. Lett. B **713**, 387 (2012).
 - [15] T. Aaltonen *et al.* (CDF Collaboration) Phys. Rev. Lett. **107**, 191801 (2011);
T. Aaltonen *et al.* (CDF Collaboration), Phys. Rev. Lett. **107**, 239903 (2011).
 - [16] V. M. Abazov *et al.*, (D0 Collaboration) Nucl. Instrum. Meth. in Phys. Res. A **565**, 463 (2006);
S. N. Ahmed *et al.*, Nucl. Instrum. and Meth. in Phys. Res. A **634**, 8 (2011);
V. M. Abazov *et al.* Nucl. Instrum. and Meth. in Phys. Res. A **552**, 372 (2005).
 - [17] Pseudorapidity η is defined as $\eta = -\ln[\tan(\theta/2)]$, where θ is the polar angle measured with respect to the proton beam direction.
 - [18] R. Angstat *et al.*, (D0 Collaboration), Nucl. Instrum. Meth. in Phys. Res. A **622**, 298 (2010).
 - [19] J. Beringer *et al.* (Particle Data Group), Phys. Rev. D **86**, 010001 (2012).
 - [20] T. Sjöstrand *et al.*, Comput. Phys. Commun. **135**, 238 (2001).
 - [21] D. J. Lange, Nucl. Instrum. Meth. in Phys. Res. A **462**, 152 (2001).
 - [22] R. Brun and F. Carminati, CERN Program Library Writeup W5013, 1993. We use GEANT version 3.15.
 - [23] Heavy Flavor Averaging Group,
<http://www.slac.stanford.edu/xorg/hfag/osc>
 - [24] R. Aaij *et al.* (LHCb Collaboration), Phys. Rev. Lett. **107**, 211801 (2011).
 - [25] A. Hoecker *et al.*, “Toolkit for Multivariate Data Analysis”, arXiv:physics/0703039v5 (2007). We use version 4.1.0.
 - [26] T. Junk, Nucl. Instrum. and Meth. in Phys. Res. A **434**, 435 (1995).